

Image-domain time-lapse inversion with extended images

Aaron Girard* (Technical University of Delft and ION Geophysical) and
Ivan Vasconcelos (ION Geophysical / GXT Imaging Solutions)

SUMMARY

Time-lapse seismic data is used to monitor subsurface changes occurring between consecutive surveys. One way to look at the differences is to create images from each survey and simply subtract them to obtain a difference. It is possible to model image differences directly from the slowness change between two surveys: this leads to a forward modeling operator that essentially performs differential migration. We further exploit the concept of image-domain time-lapse inversion by introducing extended-image time-lapse differences. Extended images are generalizations of the conventional imaging condition, and the resulting images are an extension of subsurface image gathers. We discuss objective functions for image-domain time-lapse inversion from both conventional and extended images. These depart from the more conventional approaches to time-lapse inversion whose objective functions are parameterized in the recorded data domain. By analyzing the forward operators for conventional and extended image differences, we show that the use of image extensions yields a larger data space thus offering additional constraints for time-lapse inversion. We illustrate these concepts numerically by comparing sensitivity kernels as well as inversion results from conventional versus extended time-lapse images.

INTRODUCTION

Most time-lapse inversions use differences in recorded data (Lumley, 2001; Lumley et al., 2003; Calvert, 2005). Instead of creating the image difference in the data domain, it can be done in the image domain. Time-lapse image differences can be described using differential migration operators that map the change in the model slowness to the change in the image (Sava and Biondi, 2004; Albertin et al., 2006; Maharramov and Albertin, 2007; Sava and Vlad, 2008). Inversion in the image domain behaves differently than in the data domain (de Hoop et al., 2006; Symes, 2008). In addition, a particularly important concept is the use of image extensions to expand the data space and increase redundancy in image-domain inversion (Symes 2008).

In finite-frequency data-domain inversion it is useful to analyze the behavior of sensitivity kernels (e.g., Tarantola, 1984; Tromp et al., 2005) since they are a key component of adjoint, gradient-based inversion schemes. In this paper we also analyze sensitivity kernels, but in our case the kernels are computed by backprojecting changes in extended images. Sava and Vlad (2008) describe the computation of linearized back-projections from conventional images. The kernels we show here are generalized from Sava and Vlad (2008) to account for fully extended images (Vasconcelos et al., 2009; Sava and Vasconcelos, 2009).

The purpose of this paper is to promote the use of extended images in image-domain time-lapse inversion. We first analyze the objective functions for the conventional and extended image cases, and discuss the properties of their respective forward operators using singular value decomposition. Next, using a synthetic example, we study the behavior of the finite frequency kernels from conventional and extended image changes; and finally conclude our study by comparing gradient-based inversion results from the conventional and extended image approaches.

IMAGE-DOMAIN TIME LAPSE INVERSION

Image change

If the change in an image (∂I) from one acquisition to the next is solely due to the change in slowness (∂s), then the inversion process simply involves minimizing the mean square data misfit \mathcal{J} by:

$$\mathcal{J}(\partial s) = \frac{1}{2} \|\partial I - L\partial s\|^2 \quad (1)$$

where L is a differential migration operator (e.g. Sava and Vlad, 2008) that maps ∂s to ∂I . Equation 1 implies that there is such an operator L that acts on ∂s to give the time-lapse image change, as shown by:

$$\partial I = L\partial s. \quad (2)$$

In real time-lapse experiments, however, ∂s is not known a priori. The image mapped from the baseline survey (d_0) and a later survey (d_1), are both migrated with the original background slowness (s_0) and can be subtracted to define ∂I_{true} by:

$$\partial I_{true} = \mathcal{J}(s_0)[d_1] - \mathcal{J}(s_0)[d_0]. \quad (3)$$

where s_0 , the background slowness model, is a best fit slowness model to d_0 . Subtracting two images does not necessarily yield a ∂I that is linear on ∂s , leading to a more complicated process of defining ∂I in terms of ∂s . This is seen in ∂I_{true} from equation 3 and the linearized ∂I from equation 2.

Extended images

Conventional imaging involves the cross-correlation of reconstructed source and receiver wavefields to create an image (Claerbout, 1985). It follows that offsetting the wavefields by some distance δx will also create an image as shown by Vasconcelos et al (2009) and Sava and Vasconcelos (2010), which is called an image extension. In this case the extended image is only in the horizontal space domain, which is also called a subsurface-offset common image gather (Biondi, 2006), but the same can be done to δy and δz , as well as the time domain, using time-lag τ . The new image is called an extended image (I_e). The

Image-domain time-lapse inversion with extended images

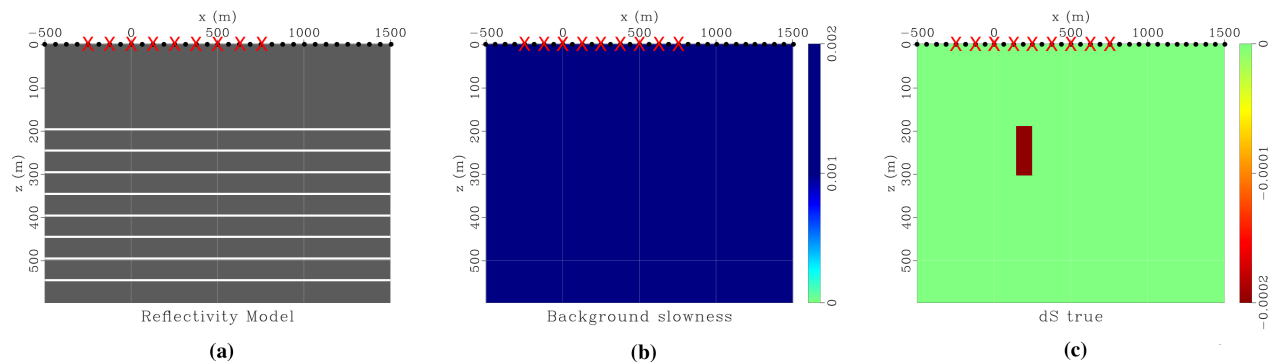


Figure 1: Model used for numerical examples. Panel (a) shows the eight reflectors at 50 meter depth intervals. Panel (b) is the homogeneous background slowness of 0.001 s/km, and panel (c) shows the true slowness change, in s/m, which is non-zero only in the box directly under the center of the shot locations. The nine shot locations are portrayed by red Xs, with a shot spacing of 125 meters, and the receivers cover the entire surface with a 5 meter spacing, as represented by black dots.

logic from a conventional image can therefore be used to invert ∂I_e for slowness ∂s with:

$$\mathcal{J}_e(\partial s) = \frac{1}{2} \|\partial I_e - L_e \partial s\|^2 \quad (4)$$

where L_e is an extended image differential migration operator acting upon ∂s . A similar condition to equation 2 follows for the creation of ∂I_e :

$$\partial I_e = L_e \partial s \quad (5)$$

which consists of introducing extended imaging conditions (Vasconcelos et al., 2009; Sava and Vasconcelos, 2010) in the differential migration calculations (e.g. Sava and Vlad, 2008).

Differential migration operator

The idea behind the use of extended images is to increase the sensitivity of the forward operator L with respect to the model ∂s . In practice, this translates to increasing the number of images corresponding to the same input model, which generates a larger data space compared to that of a conventional image. If the additional information contained in the image extensions is non-zero and linearly independent from the information in the conventional image (which is a subset of the extended image), then it follows that L_e is more sensitive to the model than L . One way to address the sensitivity of the forward operators is to use singular value decomposition (SVD):

$$L = U\Lambda V^T \quad (6)$$

where L is a matrix with size $N_m \times N_m$, with N_m being the number of model points. Both the data space eigenvectors U and model space eigenvectors V have the same dimensions as L in this case (Scales et al., 2001), since here we assumed that the conventional image has one datapoint (∂I) created for each model point (∂s). This means that the eigenvalue matrix Λ is also $N_m \times N_m$ for the conventional image case.

Likewise, the operator L_e has a size $(N_m \times N_e) \times N_m$, where N_e is the number of image extensions. This means that for

each model point there are N_e image points associated with it. Equation 6 can be modified for the extended image case:

$$L_e = U_e \Lambda_e V_e^T \quad (7)$$

which is similar to equation 6, but the extensions change the dimensions of the U_e and Λ_e matrices. The term Λ_e has the same size as L_e , but the U_e and V_e must be square, i.e. $(N_m \times N_e) \times (N_m \times N_e)$ and $N_m \times N_m$, respectively. The model eigenvector matrices V and V_e are calculated from the identical ∂s model, shown in equations 6 and 7 respectively, so it follows that $V = V_e$. The data eigenvector matrices U and U_e differ in dimensions by N_e^2 . This means that there are more data eigenvectors to span the model space. Even though not all of the eigenvectors gained in the image extensions are non-zero, the extra data space eigenvectors are responsible for the gain in model sensitivity. This can increase the convergence rate of gradient-based inversion methods. The increase in dimensions does increase the number of calculations required when using extended images, meaning that the cost of using extended images could become an obstacle in practice. However, addressing the cost increase from the use of extended images is beyond the scope of this abstract.

NUMERICAL EXAMPLES

In time-lapse imaging there is a reflector model over which seismic data is acquired in identical geometries at two different times. We assume that the reflectors, shown in figure 1(a), do not change between the two acquisitions, but the slowness model does. In this model the background slowness s_0 used, shown in figure 1(b), and the slowness change ∂s between acquisitions is shown in figure 1(c).

The data was modeled in 9 shots over the model both before and after the slowness update. A single shot record for the model before the update is shown in figure 2(a). The data for all shots was then migrated using the background slowness for both d_0 , shown in figure 2(b), and d_1 , shown in figure 2(c). The two images were subtracted, as in equation 3, to give ∂I_{true} as

Image-domain time-lapse inversion with extended images

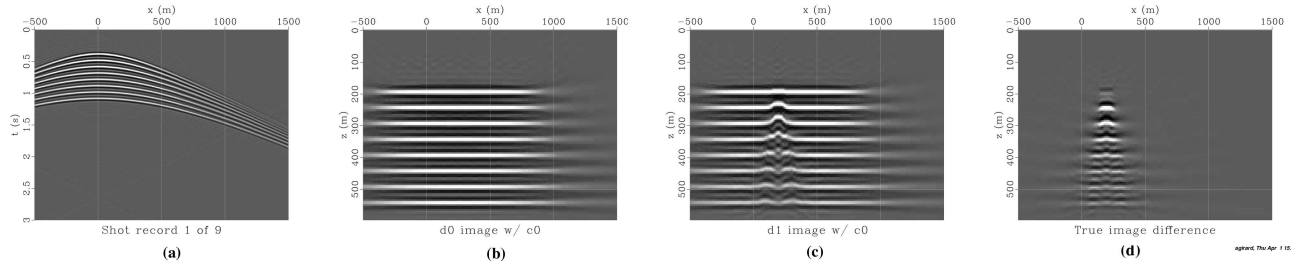


Figure 2: Panel (a) is a display of a single shot record from d_0 over the model, which is one of 9 used in creating the total image, migrated with the background slowness, as shown in panel (b). Similarly, the image migrated from d_1 with the background slowness is shown in panel (c). Panels (b) and (c) correspond to $\mathcal{S}(s_0)[d_0]$ and $\mathcal{S}(s_0)[d_1]$ respectively, to create ∂I_{true} from equation 3 which is shown in panel (d). Straight subtraction leads to panel (d), and with the model being a large slowness change with a sharp interface the result is somewhat different from the linearized image assumed in this case.

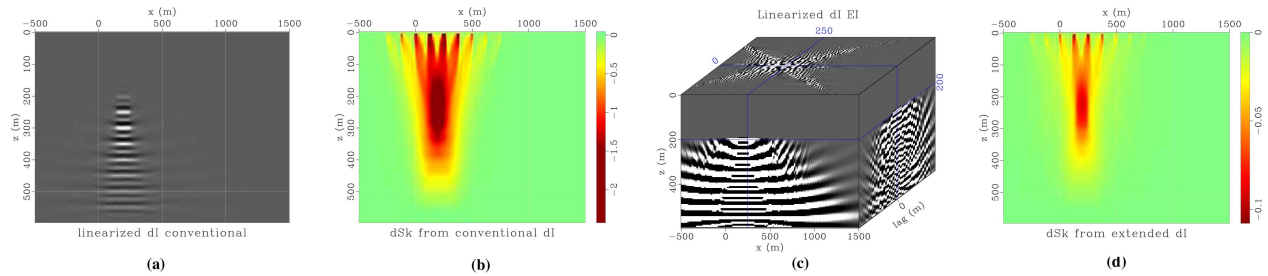


Figure 3: Panel (a) shows the linearized ∂I for the conventional image, calculated from equation 2, and panel (b) shows the corresponding kernel ∂s_k for all nine shots and all frequencies from the total ∂I . Panel (c) is a representation of the extended image from equation 5; the front side shows the zero-lag ∂I_e , the top side is a slice taken at the top of the ∂s box in figure 1, and the right side shows all lags through the same ∂s box. The ∂I_e portrays 41 lags at 50 meter intervals from $-1000 < \delta x < 1000$. Panel (d) is the corresponding ∂s_{ke} for all shots and frequencies from the entire ∂I_e . The improvement from (b) to (d) is shown both in the amplitude and location of the sensitivities. Panel (d) is closer to ∂s_{true} (figure 1c) than (b).

shown in figure 2(d). When compared to the linearized image difference in figure 3(a), which comes from equation 2, the images are not exactly the same. Some reasons for this difference include the fact that the update to the slowness was -0.002 s/m, which is equivalent to increasing the velocity 25% in the region of the update, and the fact that the sharp change generates nonlinear effects.

The extended image shown in figure 3(c) is considerably larger than the conventional image. The front face of the extended image cube is the zero-lag ($\delta x = 0$) image, which is equivalent to the conventional image in 3(a) when fit to the same scale. Each δx has a ∂I associated with it, meaning that over the range of lags $-1000 \text{ m} < \delta x < 1000 \text{ m}$ in steps of 50 meters there are 41 image extensions, making ∂I_e 41 times larger than ∂I .

Panels (b) and (d) of figure 3 are the backprojections from ∂I and ∂I_e , respectively. These sensitivity kernels ∂s_k are calculated by applying the adjoint of the differential migration operator L^\dagger to the ∂I :

$$L^\dagger \partial I = L^\dagger L \partial s = \partial s_k. \quad (8)$$

The closer $L^\dagger L$ comes to the identity matrix, the closer the adjoint operator L^\dagger comes to a pseudoinverse, meaning that U_e better spans the modelspace. The kernel is a representation of

regions to which the data for ∂I is sensitive, and an estimate of what the magnitude of ∂s is. Therefore it can be considered as the output of a first iteration of a gradient-based inversion scheme when a homogenous initial model is assumed.

The inversion scheme used is the iterative shaping regularization method by Fomel (2007). It was run over several iteration lengths to get information on how quickly the solution converged for conventional and extended images, and compare the results. The shaping operator is a triangle smoothing operator sized 20 samples in both x and z (Fomel, 2007), with 0.001 used for the weighting factor ϵ .

DISCUSSION

When comparing the kernels in panels (b) and (d) in figure 3 there are two main differences. The first noticeable difference is the scale, where panel (b) for the conventional image has a reasonable focusing on the updated slowness area, but the estimated values are nearly four orders of magnitude higher than the true ∂s . Conversely, the ∂s_k from the extended image is only two or three orders of magnitude away from the true ∂s . This means that the use of extended images has given a better first guess at the updated slowness model after a sin-

Image-domain time-lapse inversion with extended images

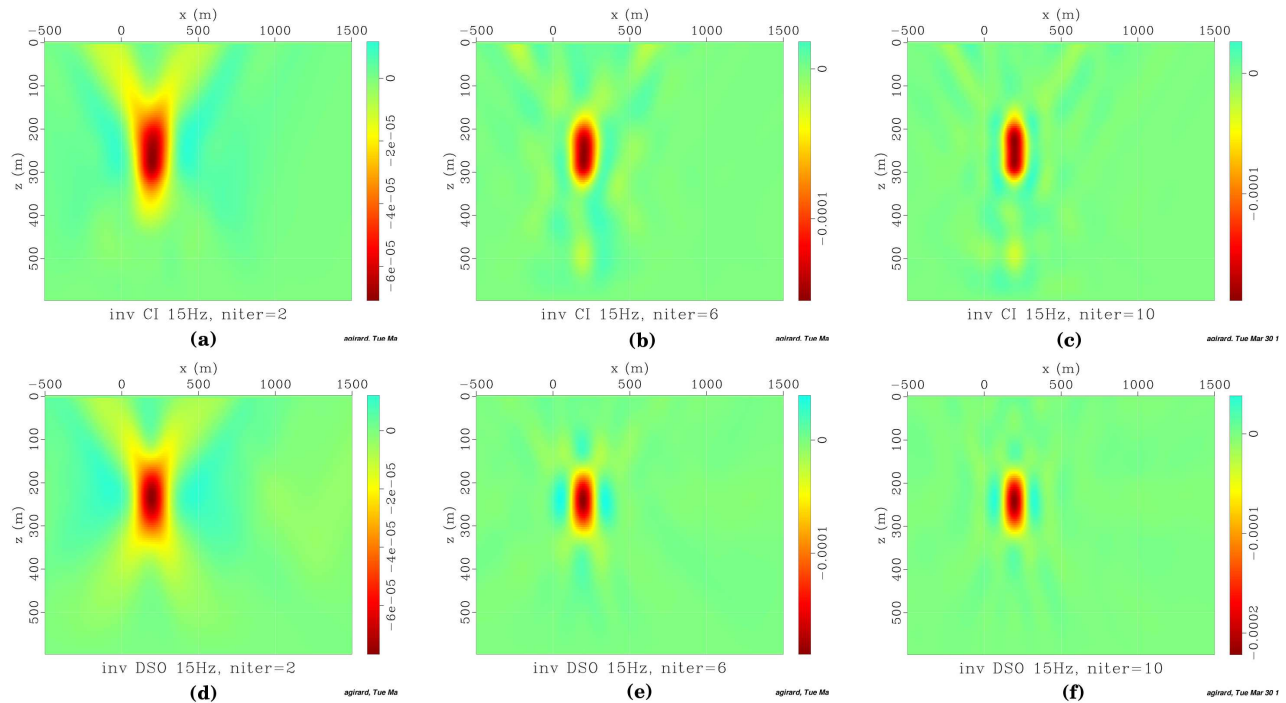


Figure 4: Inversion at 15Hz for the slowness change at different iterations. Panel (a) shows the results from the conventional image after two iterations, panel (b) after 6 iterations, and panel (c) after 10 iterations. Panels (d) through (f) show results at the same iteration steps, but from the extended image. In each panel the improvement by using extended images can be seen in both the shape and the reconstructed slowness values.

gle inversion iteration. The second difference is the shape of the sensitive region, which is larger and more smoothed in (b) than (d), proving that the kernel from the extended image is an improvement over the kernel from the conventional image. The ∂s_{ke} more closely resembles the shape and magnitude of ∂s_{true} , even with no inversion.

Inversion results after further iterations in figure 4 show the results from the conventional image for 2, 6 and 10 iterations in panels (a) through (c), respectively, and the same number of iterations from ∂I_e in panels (d) through (f). Remembering that ∂s_k and ∂s_{ke} can be thought of as the first iteration result, the second iteration of each image is an improvement. However, the extended image after two iterations in figure 4(d) shows the improvement from the use of extended images in the shape of the inverted area. Already the result from the extended image inversion in panel (d) resembles the symmetric, regular shape of ∂s_{true} , more so than the result from the conventional image in panel (a).

Further iterations show that the extended image for this single frequency of 15Hz gives a more realistic result, since the area of the slowness update is centered on the area of the true ∂s , as seen after 6 iterations in panel (e). The result from the conventional image after 6 iterations is less focused, especially in shot locations and in the deeper region, meaning that the best fit solution has either not been found or is not as good as the solution for the extended image inversion. Even after 10 iterations, shown in panel (c), the conventional image does not entirely

focus on the region of the true ∂s . Conversely, in panel (f), more iterations for the inversion from extended images does not greatly improve, meaning that it has already converged to a best-fit solution.

CONCLUSION

We show that the use of extended images improves image-domain time-lapse inversion, and that for a simple 2D case the results converge faster and closer to the true slowness update. This may prove to be a considerable improvement for more complex reflector models and slowness updates, and the cost associated with the calculation of extended images can be offset by the reduction of inversion iterations required to converge to a best-fit solution. Future work will be to use more complex models and to define where image extensions should be calculated to maximize the number of non-zero eigenvectors that map the model space while minimizing the number of required calculations.

ACKNOWLEDGEMENTS

We would like to thank ION/GXT Imaging Solutions for funding and allowing publication of this work. We also thank Kees Wapenaar at TU Delft, and Andrew Curtis and the School of Geosciences at University of Edinburgh for their contributions.

EDITED REFERENCES

Note: This reference list is a copy-edited version of the reference list submitted by the author. Reference lists for the 2010 SEG Technical Program Expanded Abstracts have been copy edited so that references provided with the online metadata for each paper will achieve a high degree of linking to cited sources that appear on the Web.

REFERENCES

- Albertin, U., P. Sava, J. Etgen, and M. Maharramov, 2006, Adjoint wave-equation velocity analysis: 76th Annual International Meeting, SEG, Expanded Abstracts.
- Biondi, B., 2006, Three Dimensional Seismic Imaging: Society of Exploration Geophysicists.
- Calvert, R., 2005, Insights and Methods for 4D Reservoir Monitoring and Characterization: SEG/EAGE.
- Claerbout, J., 1985, Imaging the Earth's Interior: Blackwell Scientific Publications, Inc.
- de Hoop, M. V., R. D. van der Hilst, and P. Shen, 2006, Wave-equation reflection tomography: annihilators and sensitivity kernels: *Geophysical Journal International*, **167**, no. 3, 1332–1352, [doi:10.1111/j.1365-246X.2006.03132.x](https://doi.org/10.1111/j.1365-246X.2006.03132.x).
- Fomel, S., 2007, Shaping regularization in geophysical-estimation problems: *Geophysics*, **72**, no. 2, R29–R36, [doi:10.1190/1.2433716](https://doi.org/10.1190/1.2433716).
- Lumley, D., 2001, Time-lapse seismic reservoir monitoring: *Geophysics*, **66**, 50–53, [doi:10.1190/1.1444921](https://doi.org/10.1190/1.1444921).
- Lumley, D., M. Meadows, S. Cole, and D. Adams, 2003, 4D seismic data processing issues and examples: 73rd Annual International Meeting, SEG, Expanded Abstracts.
- Maharramov, M., and U. Albertin, 2007, Localized image-difference wave-equation tomography: 77th Annual International Meeting, SEG, Expanded Abstracts.
- Sava, P., and B. Biondi, 2004, Wave-equation migration velocity analysis – I: Theory: *Geophysical Prospecting*, **52**, no. 6, 593–606, [doi:10.1111/j.1365-2478.2004.00447.x](https://doi.org/10.1111/j.1365-2478.2004.00447.x).
- Sava, P., and I. Vasconcelos, 2009, Efficient computation of extended images by wavefield-based migration: 79th Annual International Meeting, SEG, Expanded Abstracts.
- Sava, P., and I. Vasconcelos, 2010, Extended imaging conditions for wave-equation migration: *Geophysical Prospecting*, no. [doi:10.1111/j.1365-2478.2010.00888.x](https://doi.org/10.1111/j.1365-2478.2010.00888.x).
- Sava, P., and I. Vlad, 2008, Numeric implementation of wave-equation migration velocity analysis operators: *Geophysics*, **73**, no. 5, VE145–VE159, [doi:10.1190/1.2953337](https://doi.org/10.1190/1.2953337).
- Scales, J., M. Smith, and S. Treitel, 2001, *Introductory Geophysical Inverse Theory*: Samizdat Press.
- Symes, W. W., 2008, Approximate linearized inversion by optimal scaling of prestack depth migration: *Geophysics*, **73**, no. 2, R23–R35, [doi:10.1190/1.2836323](https://doi.org/10.1190/1.2836323).
- Tarantola, A., 1984, Inversion of seismic reflection data in the acoustic approximation: *Geophysics*, **49**, 1259–1266, [doi:10.1190/1.1441754](https://doi.org/10.1190/1.1441754).
- Tromp, J., C. Tape, and Q. Liu, 2005, Seismic tomography, adjoint methods, time reversal and banana-doughnut kernels: *Geophysical Journal International*, **160**, no. 1, 195–216, [doi:10.1111/j.1365-246X.2004.02453.x](https://doi.org/10.1111/j.1365-246X.2004.02453.x).
- Vasconcelos, I., P. Sava, and H. Douma, 2009, Wave-equation extended images via image-domain interferometry: 79th Annual International Meeting, SEG, Expanded Abstracts.